Insights into Seismogenic Deformation during the 2018 Hualien, Taiwan, Earthquake Sequence from InSAR, GPS, and Modeling

by Jiun-Yee Yen, Chih-Heng Lu, Rebecca J. Dorsey, Hao Kuo-Chen, Chung-Pai Chang, Chun-Chin Wang, Ray Y. Chuang, Yu-Ting Kuo, Chi-Yu Chiu, Yo-Ho Chang, Fabio Bovenga, and Wen-Yen Chang

ABSTRACT

We provide new data and insights into a 6 February 2018 M_w 6.4 earthquake that shook the city of Hualien in eastern Taiwan at the leading edge of a modern arc–continent collision. Fatalities and damages were concentrated near the Milun fault and extended south to the northern Longitudinal Valley fault. Although the Hualien area has one of the highest rates of seismicity in Taiwan, the geologic structures responsible for active deformation were not well understood before this event. We analyzed Interferometric Synthetic Aperture Radar (InSAR) and Global Positioning System (GPS) data and produced a 3D displacement model with InSAR and azimuth offset of radar images to document surface deformation induced by this earthquake. The 3D displacement model was inverted to estimate slip on the Milun fault. We find that models assuming a single fault are inconsistent with observations of coseismic deformation and regional strain patterns, providing evidence for linked slip on a little-studied offshore thrust belt. Based on data presented here and elsewhere, we propose a model for transpressive deformation in a zone of oblique convergence and left-lateral wrench tectonics to explain this and a prior 1951 M 7.3 earthquake.

Electronic Supplement: Tables listing of details of the satellite radar images used in this research and Global Positioning System (GPS) coseismic deformation.

INTRODUCTION

About 67 yrs after one of the largest earthquakes recorded in eastern Taiwan, the city of Hualien experienced an unusual seismic sequence that started on 4 February 2018, with an M_w 6.1 earthquake located 28 km northeast of the city. The largest event in this sequence, an M_w 6.4 earthquake with an epicenter located 10 km northeast of Hualien (Fig. 1), occurred at 23:50 p.m. local time 6 February. The M_w 6.4 event caused collapse of four large buildings, 17 fatalities, and extensive damage to roads and other infrastructure. Field surveys conducted immediately after the 6 February event (Eastern Taiwan Earthquake Center [ETEC], 2018) revealed 70 cm of transpressive left-lateral, east-side-up coseismic offset across the steeply east-dipping Milun fault and a similar amount of left-lateral displacement on the Lingding fault 10 km south of Hualien (Fig. 1). The focal mechanism of the main earthquake from U.S. Geological Survey (USGS) and Central Weather Bureau (CWB) indicates a steeply west-dipping fault plane at 10–12 km depth, in contrast to the steep eastward dip on the Milun fault documented in field and near-surface geophysical surveys (Yu, 1997). The diverging dip directions on shallow and deep levels of the seismogenic Milun fault require an explanation. The 2018 earthquake sequence illuminated a network of active faults in the Hualien area, offering a rare opportunity to document how local structures accommodate oblique relative plate motion at a complex collisional plate boundary.

The region struck by the February 2018 earthquake sequence lies in a zone of oblique arc–continent collision between the Philippine Sea plate and Eurasian continental margin (Fig. 1, inset). The steeply east-dipping Longitudinal Valley fault and a little-studied offshore thrust belt accommodate more than half of the modern oblique convergence (82 mm/yr) between the Eurasian and Philippine Sea plates (Huang *et al.*, 2010; Ching *et al.*, 2011). Prior studies document a regional change from east-dipping subduction of Eurasian lithosphere in southern and central Taiwan to a west-dipping boundary in the north, where strain is influenced by northward subduction at the Ryukyu trench (Lallemand *et al.*, 1997; Font *et al.*, 2001; Kuo-Chen *et al.*, 2012). The last major rupture on the Milun fault was an M_w 7.3 earthquake in October 1951 that produced ~1.2 m of vertical offset and ~2 m of left-lateral horizontal offset (Hsu, 1962; Shyu, 2005). Other than rare pulses of transient aseismic strain (Yen *et al.*, 2011), the Milun fault has been dormant since 1951. Shyu *et al.* (2016) proposed that the Milun fault is linked to a detachment fault at depth that separates shallow sediments

doi: 10.1785/0220180228

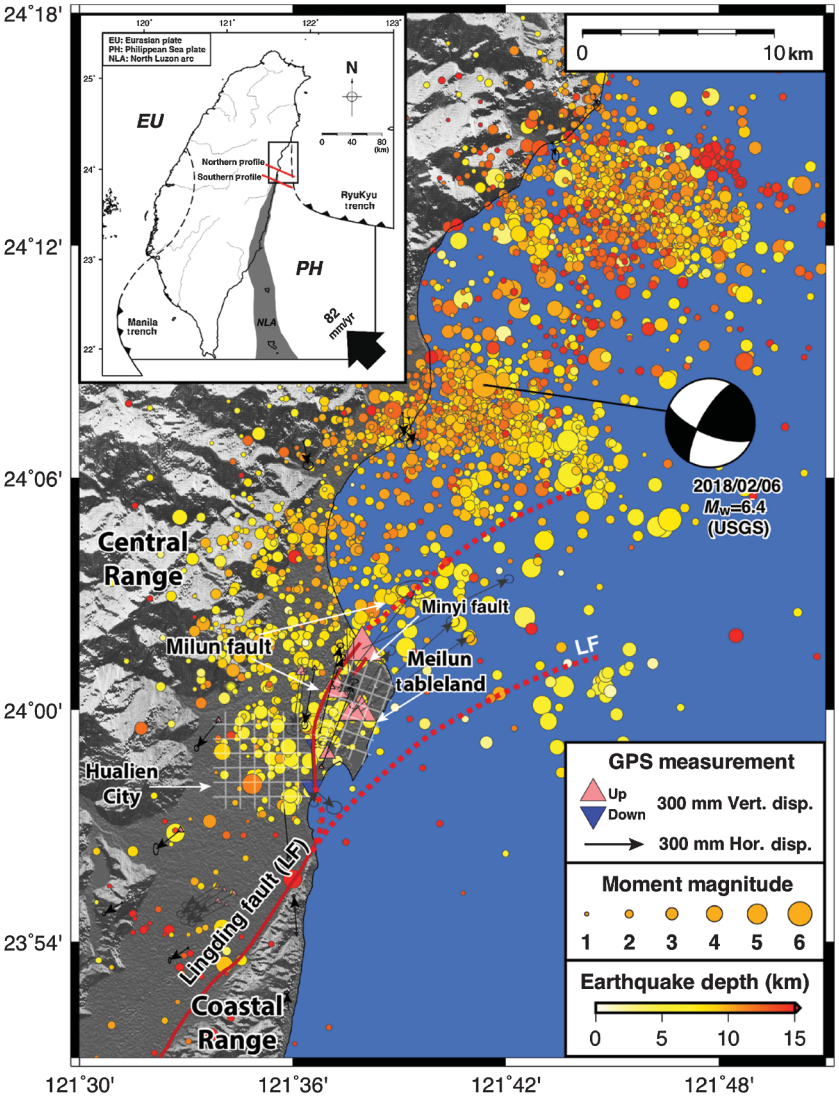

▲ **Figure 1.** (Inset) The South China Sea (Eurasian plate) is subducting eastward beneath the Philippine Sea plate along the Manila trench south of Taiwan, and the Philippine Sea plate is subducting northward beneath the Eurasian plate. Hualien is located at the northern tip of flipping of subduction polarity. Study area of 2018 Hualien earthquakes. Black arrows indicate coseismic Global Positioning System (GPS) direction. Yellow circles are earthquakes that occurred in February 2018. Red lines are Milun and Lingding faults. Both continuous (black line) and campaign GPS (gray line) show opposite motion on either side of the Milun and Lingding faults. Crustal blocks east of both faults move north relative to central Taiwan via left-lateral fault offset; the relative motion becomes more eastward because of local clockwise rotation near the north end of the Milun fault. Hash and oblique hash areas are the city of Hualien and Meilun tableland, respectively. Red lines (inset) are northern and southern profiles shown in Figure 6.

in the northern Longitudinal Valley from deeper crust of the Coastal Range as it translates north toward the Ryukyu trench. This and other models based on microseismicity and interseismic strain (e.g., Chen *et al.*, 2014) are limited by the absence of fault-rupture data that reveal important aspects of active plate-boundary deformation.

This article presents a study of coseismic surface deformation produced by the 6 February 2018 M_w 6.4 Hualien earthquake. We used Sentinel 1A/B Terrain Observation with Progressive Scan and Advanced Land Observation Satellite-2 (ALOS-2) Synthetic Aperture Radar (SAR) interferometry combined with Global Positioning System (GPS) data to document surface deformation during this event. Images from ascending and descending tracks were used to measure line-of-sight (LOS) deformation with opposing look angles, and pixel offset (PO) of ALOS-2 radar images were used to track deformation in the radar azimuth direction. We then calculated a 3D surface displacement field by combining PO and Differential Interferometric Synthetic Aperture Radar (DInSAR) results (Casu and Manconi, 2016). The data reveal consistent left-lateral displacement on the Milun and Lingding faults, with large variations in vertical motion that provide insight into fault-zone geometric complexities. Using these results, we propose a regional kinematic model to explain the relationship between driving plate motion and neotectonic deformation on seismogenic faults in this active collisional setting.

MATERIALS AND METHODS

Continuous GPS (cGPS) and campaign GPS data were used in this study. cGPS data were gathered by the CWB, Central Geological Survey, Institute of Earth Sciences of Sinica Academia, Industrial Technology Research Institute, and ETEC, and provided by the ETEC. Coseismic deformation from cGPS is the difference between the 7-day average before earthquake and 5-day average after the earthquake for most of the cGPS sites. For the sites affected by the 4 February 2018 earthquake, coseismic deformation was the position differences between two days before the 6 February main event and seven days after the earthquake. Campaign GPS data were the difference between May 2017 and February 2018 (Fig. 1). GAMIT software was used in all the GPS solution (Herring *et al.*, 2015; see the Ⓔ electronic supplement available to this article).

DInSAR is an excellent tool with which to measure a displacement field over a large area and has been applied to various cases of surface deformation since the 1990s (Massonnet and Feigl, 1998; Bürgmann *et al.*, 2000; Wright *et al.*, 2004). In this study, we processed data from ascending and descending radar images acquired from Sentinel-1 A/B satellites launched by European Space Agency (ESA) and ALOS-2 satellite launched by JAXA (see the Ⓔ electronic supplement available to this article). The DInSAR phase in each pixel contains several different types of phase difference between master and slave images. By removing

unwanted contributions such as those related to topography, orbit, and atmosphere, we are left with useful deformation signals. GMTSAR software (Sandwell *et al.*, 2011) was used for InSAR processing, which included removal of orbit ramp and topographic phase by precise orbit from ESA and ALOS 15 m digital elevation model (see Data and Resources), respectively. SNAPHU software was used for unwrapping interferograms to the LOS displacement field (Chen and Zebker, 2002).

Because we have both ascending and descending track radar images from Sentinel-1 and ALOS-2 radar satellites, it is theoretically possible to solve for 3D displacement field (north, east, and vertical) from four LOS displacements with different satellite flight directions. However, the two satellites have similar ground tracks that are less than 25° between ground-track angles and the north direction, so the resulting north–south component of displacement field is often poorly constrained. The 3D displacement field is more readily understood than the LOS displacement field and is essential for understanding surface deformation caused by this earthquake. Using PO method, the horizontal displacement field along both azimuth and range directions can be estimated with precision that depends on the spatial resolution. In the present case, the PO displacement estimation along azimuth is particularly useful because it allows constraining the north–south component of displacement field. Therefore, we applied PO method on ALOS-2 SAR images, which has an azimuth resolution better than Sentinel-1. The relative offset is measured by calculating the correlation between preseismic and postseismic images of the same spatial resolution (Leprince *et al.*, 2007). The PO method is chosen to solve an image registration problem (Zitová and Flusser, 2003), and offsets are recorded when cross correlation between preseismic and postseismic image patches is maximum (Leprince *et al.*, 2007). This technique has been successfully applied in other studies that obtained coseismic offsets from satellite optical images (Van Puymbroeck *et al.*, 2000; Michel and Avouac, 2002; Klinger *et al.*, 2006), aerial photos (Michel and Avouac, 2002), and SAR amplitude images (Fialko *et al.*, 2001).

We constructed coseismic 3D displacement model using corrected LOS displacement from both ALOS-2 and Sentinel-1 (from both ascending and descending direction) and azimuth offset (from both ascending and descending) in the north–south direction to solve for the 3D displacement field. LOS displacements were compared with coseismic GPS projected to LOS direction for both satellites in both ascending and descending directions (Fig. 2), and the slopes for all datasets were adjusted to 1. The corrected LOS displacements were combined with azimuth offsets to solve for the 3D displacement model:

$$AZ_A = \sin\alpha_A \times \Delta_E + \cos\alpha_A \times \Delta_N \quad (1)$$

$$AZ_D = \sin\alpha_D \times \Delta_E + \cos\alpha_D \times \Delta_N \quad (2)$$

$$LOS_A = -\sin\theta_A \cos\alpha_A \times \Delta_E + \sin\theta_A \times \sin\alpha_A \times \Delta_N + \cos\theta_A \times \Delta_U \quad (3)$$

$$LOS_D = -\sin\theta_D \cos\alpha_D \times \Delta_E + \sin\theta_D \times \sin\alpha_D \times \Delta_N + \cos\theta_D \times \Delta_U, \quad (4)$$

in which α is the satellite flight direction; θ is the look angle; the capital letters A and D are ascending and descending orbit, respectively; AZ_A and AZ_D are displacements along the azimuth direction, respectively; and LOS_A and LOS_D are displacements along the range direction, respectively. Δ is surface displacement along east–west (E), north–south (N), and vertical (U) directions. Because the number of equations is greater than the number of unknowns, we solve it using the least-squares method and estimate the 3D displacement.

RESULTS

DInSAR results from Sentinel-1 and ALOS-2 are shown in Figure 2a–d. Because of differences in wavelengths, interferograms of Sentinel-1 and ALOS-2 have different numbers of fringes, but their patterns are consistent. In particular, the Sentinel-1 is more suitable for measuring small deformation than ALOS-2, which on the contrary, is well suited for catching steep spatial deformation gradient, as those occurring across faults. In the present case, the maximum detectable spatial deformation rate for ALOS-2 is about 13 times higher than for Sentinel-1 along azimuth direction and 3 times higher along range direction. Therefore, Sentinel-1 DInSAR phase is exposed to phase aliasing and consequently to phase unwrapping errors. This issue is further worsened by considering that, generally, inteferometric coherence is better for L-band data (ALOS-2) than for C-band (Sentinel-1). Therefore, the differences between Sentinel-1 and ALOS-2 displacement profiles in Figure 2 occurring mainly across the faults can be explained in terms of phase unwrapping errors affecting the Sentinel-1 data, where spatial displacement rate is high. Scatter plots in Figure 2 compared DInSAR and GPS data projected to the respective LOS direction. For InSAR results from ascending track, GPS and InSAR data generally agree with each other with a slope near 1. On the contrary, for descending track results, DInSAR often underestimated surface deformation, mostly because of the aforementioned deformation gradient exceeding radar resolving power. The data show that coseismic surface deformation was concentrated in and around city of Hualien, on and near the Milun fault. The rupture extended south to the northern Lingding fault, a strand of the Longitudinal Valley fault zone that separates the Coastal Range and the Longitudinal Valley (e.g., Lin *et al.*, 2009).

To better quantify the slant range deformation observed by radar satellites, we constructed four profiles extracted from the Sentinel-1 and ALOS-2 results to illustrate complex variations in coseismic vertical displacements (Fig. 3). Profile A shows up to 100 mm of coseismic vertical offset across the Milun fault, with deformation concentrated in a very narrow belt. Large discrepancies between ascending tracks of Sentinel-1 and ALOS-2 data are highlighted with blue arrows in profile A. The difference is due to difference in radar wavelengths

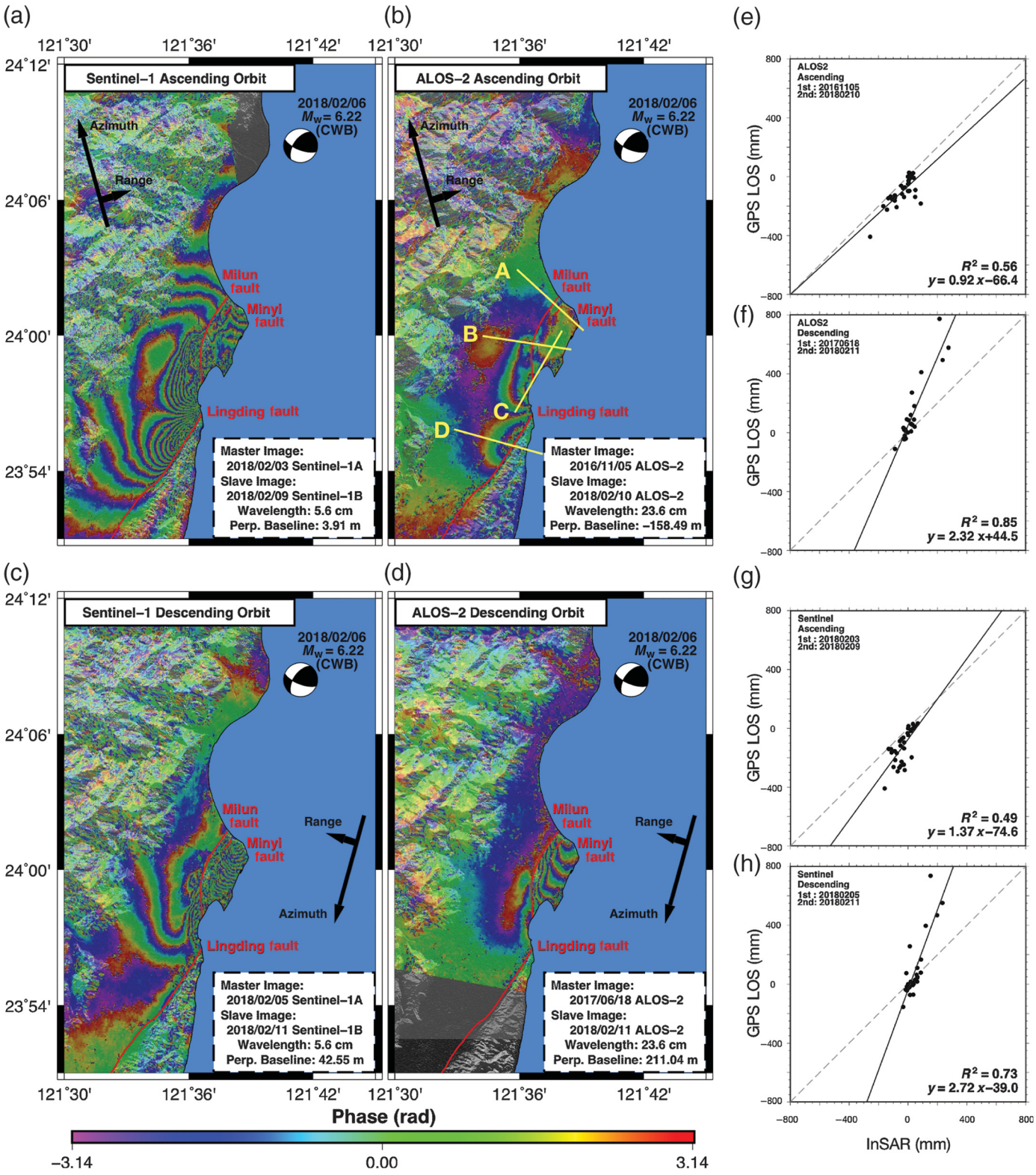

▲ **Figure 2.** (a–d) Coseismic interferograms from Sentinel-1 and Advanced Land Observation Satellite-2 (ALOS-2) radar satellites. Deformation patterns are similar for both satellites with either ascending tracks or descending track images, albeit with different number of fringes due to longer wavelength for ALOS-2. Area affected by the 2018 earthquake extends from northern tip of the Milun fault, the city of Hualien, and the northern ~10 km of the Coastal Range; line of sight (LOS) deformation and topography along profiles A, B, C, and D in (b) will be shown in Figure 3. (e–h) Comparisons of GPS data projected to radar LOS and Interferometric Synthetic Aperture Radar (InSAR). Horizontal axes are InSAR and vertical axes are GPS (LOS) data.

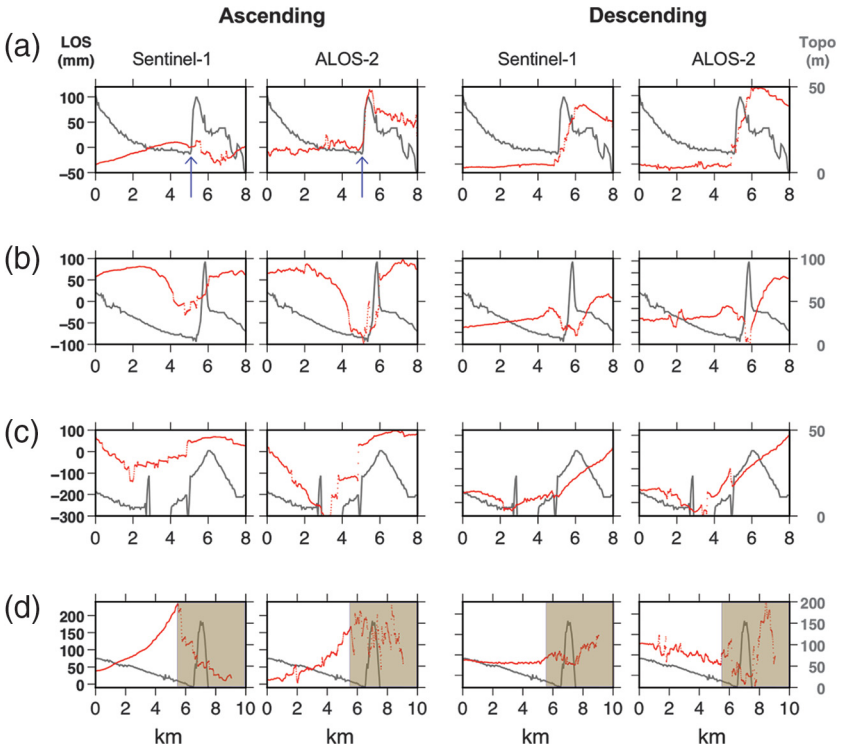

▲ **Figure 3.** (a–d) LOS surface deformation (red lines) along profiles A, B, C, and D (locations in Fig. 2b), respectively. Gray color denotes topography along the profiles.

and extremely narrow deformation zone causing a large deformation gradient. The discrepancies are less exemplified in the descending track DInSAR results; this is mainly because the azimuth direction in the ascending track is more parallel to the northern Milun fault (Fig. 2), making ascending track DInSAR not sensitive to the deformation in northern Milun fault. Profile B displays roughly 50–100 mm of deformation in a 1- to 2-km-wide fault zone (depending on satellite flight direction). In profile C, the Milun fault seems to split into two or three branches, each with several tens of millimeters of LOS deformation across fault branches in a 3-km-wide belt. Areas east of the Milun fault experienced large coseismic uplift ranging from several centimeters on the west side of the Meilun tableland to more than 30 cm on the east side of the tableland. In contrast, areas west of the Milun fault experienced much less uplift, varying from several centimeters near the fault to < 1 cm away from the fault. The differences in vertical motion reflect systematic east-side-up coseismic offset across the Milun fault, a pattern that is verified with field observations (ETEC, 2018). The area between the Milun and Lingding faults subsided by up to 30 cm, areas to the west and in the Longitudinal Valley experienced slight coseismic uplift (~1 cm), and the northernmost Coastal Range subsided slightly (Fig. 2). From profile D, the Longitudinal Valley moved toward the satellites up to 150 mm in ascending tracks, indicating higher uplifting and southward motion toward the Lingding fault. Descending tracks reveal very little movement in the Longitudinal Valley, indicating very small east–west motion. The radar coherence is low between 5 and 10 km along the profile D, which introduced large error during unwrapping in this region.

The 3D displacement model in Figure 4 was calculated by combining azimuth offsets calculated from ALOS-2 data and corrected LOS displacement from both ALOS-2 and Sentinel-1 data (see Materials and Methods section). The 3D displacement model compared well with GPS in all three directions (EW, NS, and UD) with slope ranges from 0.82 to 1.22 and R^2 near 0.8. This 3D displacement model shows that whereas areas east of the Milun and Lingding faults moved to the north, areas west of these two faults moved south (Figs. 1 and 2). The northern Meilun tableland was uplifted more than the south and southwest, producing a systematic overall southward tilt that broadly mimics the topography of the northern tableland. The Meilun tableland also experienced significant coseismic clockwise rotation roughly parallel to the curved geometry of the Milun fault (Fig. 2). Both the 3D model and GPS data show that displacements were smaller near the south-central part of the Milun fault on the Meilun tableland and increase to the east and northeast away from the fault. This is in sharp contrast to displacement west of the Lingding fault, where displacement increases toward the fault. This suggests that additional subsidiary faults contribute to the total deformation observed in the Meilun tableland.

To characterize the coseismic movement of the Milun fault based on our geodetic observations around the city of Hualien, we inverted the 3D surface displacement model (Fig. 4) to estimate fault slip (Fig. 5). Because our geodetic observations of coseismic displacements derived from GPS and InSAR are mostly limited to the area around downtown city of Hualien, the data are inherently suitable for resolving shallow fault movement of the Milun fault. We constructed a model fault following the fault trace of the Milun fault from Shyu *et al.* (2016) and modified the geometry around downtown Hualien based on field investigations of S. Y. Huang *et al.* (unpublished manuscript, 2018, see Data and Resources). We discretized the fault plane into 800 subfaults (40 along strike and 20 down-dip) with a dip angle of 70° and a depth of 5 km. We presume that the Milun fault is a high-angle east-dipping fault based on geologic records (Yu, 1997). We tested fault dip between 70° and 90° and found no obvious difference. The general dip direction varies along the strike and is perpendicular to the fault strike of each fault patch. Because we only focus on near-field displacements, the fault depth is the fault bottom, and the fault tip is at the surface. We assigned slightly larger fault plane and examine possible fault slip on the fault plane. The smoothing parameter is determined by regular trade-off curve in the inversion. Although we tested different fault lengths, for example, extending the fault far offshore to the north and linking it to the Linding fault to the south, the results of longer faults seem

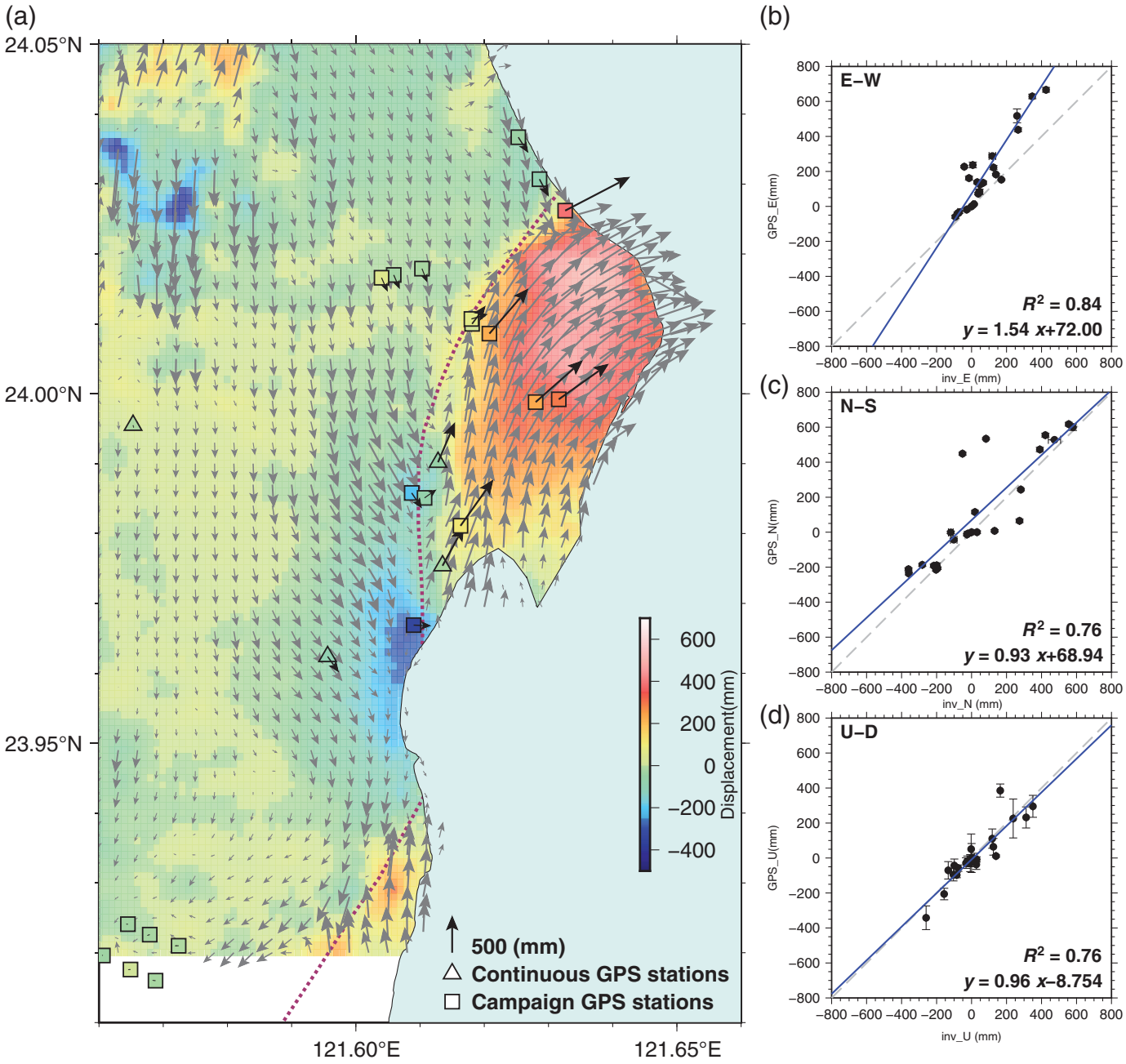

▲ **Figure 4.** (a) 3D displacement model by combining results from pixel offset results from ALOS-2 radar images of both ascending and descending tracks and coseismic radar interferometry (arrows are horizontal and color represents vertical displacement). (b–d) Comparison between displacement model and GPS results.

to be invalid because our geodetic data are too concentrated and have no ability to resolve fault slip offshore. In general, the modeled result (Fig. 5b) resembled observation (3D displacement model, Fig. 5a) in predicting displacement direction and magnitude. Residuals (Fig. 5c) were small in the west side of the study area, particularly in the horizontal directions. Vertical residuals were higher, particularly near the fault. The residual is reasonable considering lack of observation in the offshore area immediately east of the tableland. The model results show two major slip areas (Fig. 5d): one is right beneath the Meilun tableland, and the other is south of the Nanbin coastline. The magnitude of 6.32 is estimated based on the fault slip with shear modulus of 3×10^{10} N/m^2. The inversion results in general recovered first-order surface displacements with local horizontal residuals of up to 20 cm at the Meilun tableland and distributed vertical residuals of ~10 cm at the western side of the fault. The horizontal residuals result from the significant eastward motion, especially at the eastern Meilun tableland, which may be controlled by the change of the fault strike offshore. However, we have no evidence to infer the offshore fault geometry. The vertical residuals imply that there may be other structures contributing to the coseismic displacements in the footwall area.

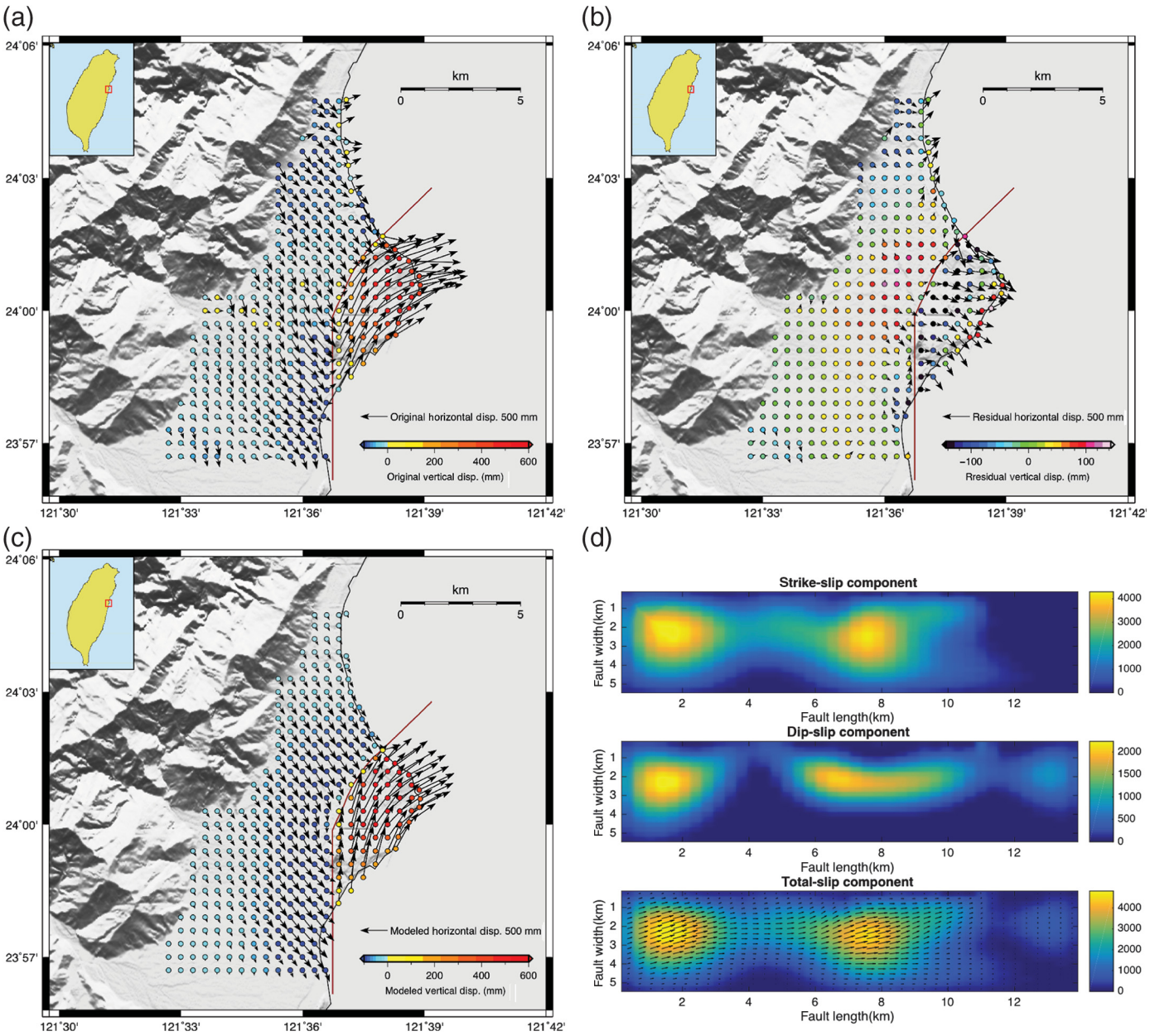

▲ **Figure 5.** Model results (see Results section for more detail). (a) Input displacement model, (b) modeled displacement, (c) residual model and observation, and (d) slip along the fault surface.

In summary, our remote-sensing and geodetic data show that the 2018 Hualien earthquake ruptured primarily along the Milun fault, and the rupture extended 20 km south of the Lingding fault. Coseismic GPS motions are consistent with surface deformation derived from DInSAR and 3D displacement model (Figs. 1, 3, and 4). Left-lateral horizontal displacement was about 70 cm on the Milun and northern Lingding faults (Figs. 1 and 2), with significant along-strike variations in vertical displacement. The crust east of the Milun fault experienced simultaneous coseismic clockwise rotation and southward tilting, with ~40 cm uplift in the north decreasing to negligible uplift in the south. A numerical rupture simulation does not replicate observed surface deformation (Fig. 5), indicating that simple geometrical fault models are not sufficient to explain the observed deformation.

DISCUSSION

About 67 yrs after the last major earthquake near the city of Hualien, the 2018 Hualien earthquake represents one of the shortest recurrence intervals for all major earthquake faults in Taiwan. This is consistent with the observation that faults in eastern Taiwan have the highest rates of modern seismicity on the island and accommodate roughly 70% of oblique convergence across the plate boundary (Hsu *et al.*, 2003; Shyu *et al.*, 2006; Huang *et al.*, 2010; Ching *et al.*, 2011). Using historical

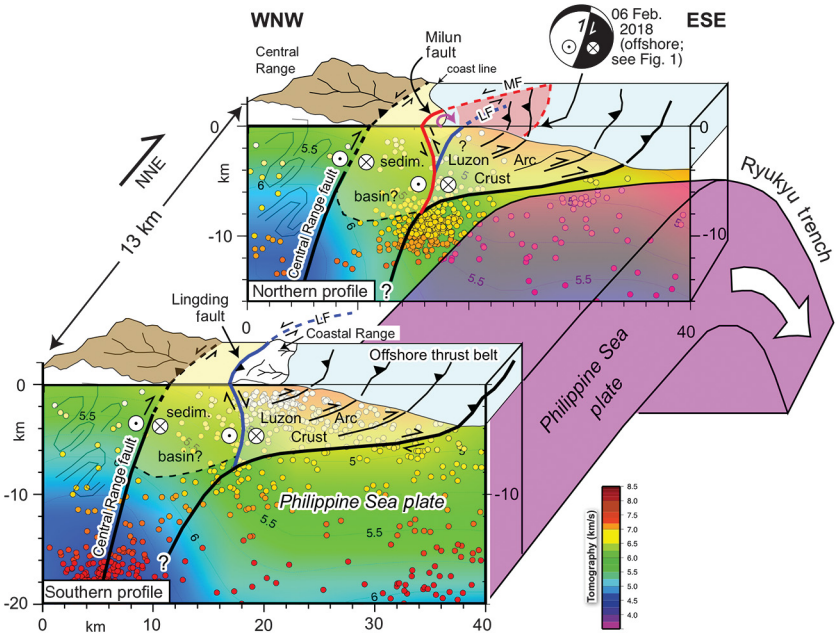

▲ **Figure 6.** Structural interpretation of faults involved in seismogenic deformation during the 6 February Hualien earthquake (focal mechanism in cross-section view), overlain on regional color tomography and seismicity (profile locations in Fig. 1, inset; seismicity from Central Weather Bureau, 1990–2015). Discordant vertical displacements on the Milun and Lingding faults indicate that they are separate strands of a regional fault network that accommodates oblique left-lateral convergence between Eurasian crust (Central Range), Luzon arc crust in a large offshore thrust belt, and oceanic crust of the Philippine Sea plate. Northward subduction of the Philippine Sea plate into the Ryukyu trench flexes the plate downward, causing subsidence and reduction of topography in the northern Coastal Range. See Discussion section.

records and original seismic data, Cheng *et al.* (2010) concluded that the 1951 $M_w \sim 7$ earthquake was located offshore northeast of city of Hualien, similar to the 2018 event, and that Hualien experienced subsidence during that event. In contrast, Lo *et al.* (2012) used 1951 tide-gauge data from Hualien harbor to suggest that the 1951 epicenter was located onshore on the Milun fault and that the city experienced 255 mm of coseismic uplift (not subsidence). Scattered field investigations from 1951 document many similarities to the 2018 event. For example, the northern segment of the Milun fault underwent 1.2 m of uplift and 2 m of horizontal offset during the 1951 earthquake, and damage along the Milun fault extended through the city of Hualien into the sea south of the Meilun Hsi river mouth (Yu, 1997). The 2018 earthquake produced a similar rupture pattern with smaller displacements up to ~70 cm of horizontal offset and 50 cm uplift on the Milun and Lingding faults. The strong similarities in fault-rupture pattern and kinematic behavior show that the 2018 event is a recurring earthquake.

Focal mechanism solutions from CWB and USGS show that the earthquake occurred at a depth of ~10–12 km on a steeply west-dipping oblique sinistral-reverse fault that coincides with the northern offshore continuation of the Milun fault (Fig. 1). Onland, however, the Milun fault dips steeply to the east (Yu, 1997; Chen *et al.*, 2014). The area east of the fault has been uplifted over time to form the Meilun tableland and Meilun hill, with a documented Holocene uplift rate of ~5 mm/yr (Yamaguchi and Ota, 2004). The area east of the Milun fault was uplifted much more than the west side during the 2018 event (Figs. 1 and 2), producing an east-side-up reverse-sense of offset on the fault. Thus, the geologic and geodetic data appear to contradict the seismic data: coseismic strain is expressed at the surface as slip on an east-dipping oblique-reverse fault, but the focal mechanism solution suggests slip on a west-dipping oblique-reverse fault in the subsurface. This apparent contradiction can be reconciled by considering the role of strike-slip fault kinematics and fault-zone geometric complexities in a 3D strain field (below). Our numerical model (Fig. 5) illustrates that a simple model can predict surface deformation near the city of Hualien, albeit with relatively large residuals in part of the study area. Lack of offshore observation and the structural complexity associated with the 2018 Hualien earthquake may be the contributing factors to the less than optimal modeling results.

Based on surface deformation documented earlier and known geologic structures in the region, we propose a structural and kinematic model that can reconcile apparent discrepancies between geodetic and seismic signals generated by the 2018 Hualien earthquake (Fig. 6). Transpressive sinistral offset on the Milun and Lingding faults is driven by regional oblique convergence at the north-northeast-trending collisional plate boundary (Fig. 1, inset). Coseismic left-lateral offset with no vertical displacement on the Lingding fault, in contrast to pronounced uplift across the northern Milun fault during the same event, indicates that these faults are independent strands of this fault zone. The Milun fault and offshore segment of the Lingding fault thus define a wedge-shaped crustal block defined by the area of observed coseismic clockwise rotation and southward tilting (Figs. 1 and 6). We infer that rotation and tilting are produced by left-lateral translation and torque applied to the fault block as a result of forced slip on curved horsetail splays in a zone of complex wrench tectonics, similar to complex 3D strain fields documented in other transpressive fault systems (Wakabayashi *et al.*, 2004; Spotila *et al.*, 2007; Sylvester *et al.*, 2011).

An important but little-studied east-vergent thrust belt directly offshore of eastern Taiwan accommodates a large fraction of convergent strain between the Philippine Sea plate and Taiwan orogen (Huang *et al.*, 2010; Ching *et al.*, 2011; Hsieh *et al.*, 2016). We suggest that the steeply east-dipping Milun and Lingding faults steepen downward into a subvertical strike-slip fault zone that may provide a backstop to the offshore thrust belt, with an uncertain relationship to the Central Range fault at depth (Fig. 6). Northward subduction of the Philippine Sea plate into the Ryukyu trench flexes the plate downward, result-

ing in subsidence and progressive reduction of topography in the northern Coastal Range (Figs. 1 and 6; Ching *et al.*, 2011; Shyu *et al.*, 2016). Despite existing uncertainties, our interpretation highlights the importance of strike-slip faults and 3D plate interactions at this oblique collisional boundary (Lallemand *et al.*, 1997; Font *et al.*, 2001; Lallemand *et al.*, 2001). Coseismic surface deformation produced by the 2018 Hualien earthquake sequence thus provides critical new insights into the local and regional kinematics of this active-fault system.

CONCLUSIONS

The 2018 M_w 6.4 Hualien earthquake in eastern Taiwan produced major surface ruptures on the Milun and Lingding faults in a zone of ongoing oblique arc–continent collision. These two faults were previously considered as different fault systems previously, but coseismic deformation documented in this study shows that they slipped in similar fashion and magnitude suggesting they are linked strands in the same fault zone.

InSAR, GPS, and 3D displacement model analyses show that much of the Meilun tableland uplifted several tens of centimeters (up to 45 cm) and moved northeast about 50 cm during this event. Areas west of the Milun and Lingding faults experienced southward motion and smaller-magnitude uplift, producing oblique left-lateral reverse offset on the Milun fault. We propose a structural model that can explain most of the observations from this earthquake and reconciles deformation patterns observed at the surface with fault slip at depth based on seismic data.

The 2018 Hualien earthquake produced a pattern of ruptures and damage along the Milun fault very similar to a 1951 M_w 7.3 earthquake in the same place. Little damage was reported along the Lingding fault during the 1951 event, possibly due to a lack of surveys because of the low population density and infrastructure along the Lingding fault at that time. The results of this study show that the Milun and Lingding faults represent an ongoing high-seismic risk, with one of the shortest recurrence intervals (67 yrs) documented on all active ground-rupturing faults in Taiwan.

DATA AND RESOURCES

The C-band Sentinel-1 A/B data are provided by the European Space Agency (ESA). Part of Global Positioning System (GPS) data are provided by Central Weather Bureau (CWB). Generic Mapping Tools (GMT; Wessel *et al.*, 2013) are used to produce several figures. The other data about digital elevation model can be found at doi: 10.5067/Z97HFCNKR6VA. The unpublished manuscript by S. Y. Huang, J. Y. Yen, B. L. Wu, I. C. Yen, and Y. C. Ray (2018), "Investigating theMilun fault: The coseismic surface rupture zone of the 2018 Hualien earthquake, Taiwan," submitted to *Terr. Atmos. Ocean. Sci.*

ACKNOWLEDGMENTS

This work was partially supported by the Ministry of Science and Technology (MOST), Taiwan. The authors thank Juliet Biggs and other anonymous reviewers for constructive review of the article.

REFERENCES

Bürgmann, R., P. A. Rosen, and E. J. Fielding (2000). Synthetic Aperture Radar Interferometry to measure Earth's surface topography and its deformation, *Annu. Rev. Earth Planet. Sci.* **28,** 169–209.

Casu, F., and A. Manconi (2016). Four-dimensional surface evolution of active rifting from spaceborne SAR data, *Geosphere* **12,** 697–705.

Chen, C. W., and H. A. Zebker (2002). Phase unwrapping for large SAR interferograms: Statistical segmentation and generalized network models, *IEEE Trans. Geosci. Remote Sens.* **40,** 1709–1719.

Chen, C. Y., J. C. Lee, Y. G. Chen, and R. F. Chen (2014). Campaigned GPS on present-day crustal deformation in northernmost Longitudinal Valley preliminary results, Hualien Taiwan, *Terr. Atmos. Ocean. Sci.* **25,** 337–357.

Cheng, S. N., Y. T. Yeh, and M. S. Yu (2010). The 1951 Taitung earthquake in Taiwan, *J. Geol. Soc. China* **39,** 267–285.

Ching, K. E., M. L. Hsieh, K. M. Johnson, K. H. Chen, R. J. Rau, and M. Yang (2011). Modern vertical deformation rates and mountain building in Taiwan from precise leveling and continuous GPS observations, 2000–2008, *J. Geophys. Res.* **116,** no. B08406, doi: 10.1029/2011JB008242.

Eastern Taiwan Earthquake Center (ETEC) (2018). Preliminary report on 20180206 Hualien earthquake, Eastern Taiwan Earthquake Center, National Dong Hwa University, available at https://etec.ndhu.edu.tw/page2_1_20180208.html (last accessed May 2018).

Fialko, Y., M. Simons, and D. Agnew (2001). The complete (3-D) surface displacement field in the epicentral area of the 1999 M_w 7.1 Hector Mine earthquake, California, from space geodetic observations, *Geophys. Res. Lett.* **28,** 3063–3066.

Font, Y., C. S. Liu, P. Schnurle, and S. Lallemand (2001). Constraints on backstop geometry of the southwest Ryukyu subduction based on reflection seismic data, *Tectonophysics* **333,** 135–158.

Herring, T. A., R. W. King, M. A. Floyd, and S. C. McClusky (2015). *Introduction to GAMIT/GLOBK, Release 10.6*, Massachusetts Institute of Technology, Cambridge, Massachusetts.

Hsieh, Y. H., J. Suppe, C. S. Liu, and S. Carena (2016). The deep structure of retrowedge thrust belts: New insight from Taiwan and the role of secondary subduction, *EGU General Assembly Conference Abstracts*, Vol. 18, EGU2016–11003.

Hsu, T. L. (1962). A study on the coastal geomorphology of Taiwan, *Proc. Geol. Soc. China* **5,** 29–45.

Hsu, Y. J., M. Simons, S. B. Yu, L. C. Kuo, and H. Y. Chen (2003). A two-dimensional dislocation model for interseismic deformation of the Taiwan mountain belt, *Earth Planet. Sci. Lett.* **211,** 287–294.

Huang, W. J., K. M. Johnson, J. Fukuda, and S. B. Yu (2010). Insights into active tectonics of eastern Taiwan from analyses of geodetic and geologic data, *J. Geophys. Res.* **115,** 161.

Klinger, Y., R. Michel, and G. C. P. King (2006). Evidence for an earthquake barrier model from $M_w \sim 7.8$ Kokoxili (Tibet) earthquake slip-distribution, *Earth Planet. Sci. Lett.* **242,** 354–364.

Kuo-Chen, H., F. T. Wu, and S. W. Roecker (2012). Three-dimensional P velocity structures of the lithosphere beneath Taiwan from the analysis of TAIGER and related seismic data sets, *J. Geophys. Res.* **117,** no. B6, doi: 10.1029/2011JB009108.

Lallemand, S., Y. Font, H. Bijwaard, and H. Kao (2001). New insights on 3-D plates interaction near Taiwan from tomography and tectonic implications, *Tectonophysics* **335,** 229–253.

Lallemand, S. E, C. S. Liu, and Y. Font (1997). A tear fault boundary between the Taiwan orogen and the Ryukyu subduction zone, *Tectonophysics* **274,** 171–190.

Leprince, S., S. Barbot, F. Ayoub, and J. P. Avouac (2007). Automatic and precise orthorectification, coregistration, and subpixel correlation of

satellite images, application to ground deformation measurements, *IEEE Trans. Geosci. Remote Sens.* **45,** 1529–1558.
Lin, C. W., W. S. Chen, Y. C. Liu, and P. T. Chen (2009). Active faults of eastern and southern Taiwan, *Special Publication of Central Geological Survey*, Vol. 23, MOEA.
Lo, C. L., E. T. Chang, and B. F. Chao (2012). Relocating the historical 1951 Hualien earthquake in eastern Taiwan based on tide gauge record, *Geophys. J. Int.* **192,** 854–860.
Massonnet, D., and K. L. Feigl (1998). Radar interferometry and its application to changes in the Earth's surface, *Rev. Geophys.* **36,** 441–500.
Michel, R., and J. P. Avouac (2002). Deformation due to the 17 August Izmit, Turkey earthquake measured from SPOT images, *J. Geophys. Res.* **107,** no. B4, doi: 10.1029/2000JB000102.
Sandwell, D. T., R. Mellors, X. Tong, M. Wei, and P. Wessel (2011). *GMTSAR: An InSAR Processing System Based on Generic Mapping Tools: Manual*, 1 pp.
Shyu, J. B. H. (2005). Neotectonic architecture of Taiwan and its implications for future large earthquakes, *J. Geophys. Res.* **110,** no. B08402, doi: 10.1029/2004JB003251.
Shyu, J. B. H., C. F. Chen, and Y. M. Wu (2016). Seismotectonic characteristics of the northernmost Longitudinal Valley, eastern Taiwan: Structural development of a vanishing suture, *Tectonophysics* **692,** 295–308.
Shyu, J. B. H., K. Sieh, J. P. Avouac, W. S. Chen, and Y. G. Chen (2006). Millennial slip rate of the Longitudinal Valley fault from river terraces: Implications for convergence across the active suture of eastern Taiwan, *J. Geophys. Res.* **111,** no. B08403, doi: 10.1029/2005JB003971.
Spotila, J. A., N. Niemi, R. Brady, M. House, J. Buscher, and M. Oskin (2007). Long-term continental deformation associated with transpressive plate motion: The San Andreas fault, *Geology* **35,** 967–970.
Sylvester, Z., C. Pirmez, and A. Cantelli (2011). A model of submarine channel-levee evolution based on channel trajectories: Implications for stratigraphic architecture, *Mar. Pet. Geol.* **28,** 716–727.
Van Puymbroeck, N., R. Michel, R. Binet, J. P. Avouac, and J. Taboury (2000). Measuring earthquakes from optical satellite images, *Appl. Optic.* **39,** 3486–3494.
Wakabayashi, J., J. V. Hengesh, and T. L. Sawyer (2004). Four-dimensional transform fault processes: Progressive evolution of step-overs and bends, *Tectonophysics* **392,** 279–301.
Wessel, P., W. H. F. Smith, R. Scharroo, J. F. Luis, and F. Wobbe (2013). Generic Mapping Tools: Improved version released, *Eos Trans. AGU* **94,** 409–410.
Wright, T. J., B. E. Parsons, and Z. Lu (2004). Toward mapping surface deformation in three dimensions using InSAR, *Geophys. Res. Lett.* **31,** L01607, doi: 10.1029/2003GL018827.
Yamaguchi, M., and Y. Ota (2004). Tectonic interpretations of Holocene marine terraces, east coast of Coastal Range, Taiwan, *Quaternary Int.* **115/116,** 71–81.
Yen, J. Y., C. H. Lu, C. P. Chang, A. J. Hooper, Y. H. Chang, W. T. Liang, T. Y. Chang, M. S. Lin, and K. S. Chen (2011). Investigating active deformation in the northern Longitudinal Valley and city of Hualien in eastern Taiwan using persistent scatterer and small-baseline SAR interferometry, *Terr. Atmos. Ocean. Sci.* **22,** 291–304.
Yu, M. S. (1997). Study on Active Faults in the Longitudinal Valley, *Ph.D. Dissertation*, National Taiwan University, 140 pp.
Zitová, B., and J. Flusser (2003). Image registration methods: A survey, *Image Vis. Comput.* **21,** 977–1000.

Jiun-Yee Yen
Chun-Chin Wang
Yo-Ho Chang
Wen-Yen Chang
Department of Natural Resource and Environmental Studies
National Dong Hwa University
No. 1, Section 2, Da Hsueh Road
Shoufeng
Hualien 97401, Taiwan
jyyen@gms.ndhu.edu.tw

Chih-Heng Lu[1]
Institute of Applied Geology
National Central University
No. 300, Zhongda Road
Zhongli District
Taoyuan City 32001, Taiwan

Rebecca J. Dorsey
Department of Earth Sciences
University of Oregon
100 Cascade Hall, 1272
Eugene, Oregon 97403-1272 U.S.A.

Hao Kuo-Chen
Chi-Yu Chiu
Department of Earth Sciences
National Central University
No. 300, Zhongda Road
Zhongli District
Taoyuan City 32001, Taiwan

Chung-Pai Chang
Center for Space and Remote Sensing Research
National Central University
No. 300, Zhongda Road
Zhongli District
Taoyuan City 32001, Taiwan

Ray Y. Chuang[2]
Department of Geography
National Taiwan University
No. 1, Section 4, Roosevelt Road
Taipei 10617, Taiwan

Yu-Ting Kuo
Institute of Earth Sciences
Academia Sinica
128 Academia Road, Section 2
Nankang
Taipei 11529, Taiwan

Fabio Bovenga
Institute for Electromagnetic Sensing of the Environment
National Research Council
Via Amendola, 122/d
70126 Bari
Italy

[1] Also at Institute for Electromagnetic Sensing of the Environment, National Research Council, Via Amendola, 122/d - 70126 Bari, Italy.
[2] Also at Research Center for Future Earth, National Taiwan University, No. 1, Section 4, Roosevelt Road, Taipei, Taiwan.